Design and Analysis of a New Doubly Salient Permanent Magnet Motor

Ming Cheng, K. T. Chau, *Member, IEEE*, and C. C. Chan, *Fellow, IEEE*

***Abstract*—This paper presents the design and analysis of a new doubly salient permanent magnet (DSPM) motor. The corresponding output power equation is analytically derived. The initial calculation of motor dimensions and parameters, namely, the core diameter, stack length, permanent magnet size, and winding turns, are also discussed. An 8/6-pole DSPM motor is designed and built for exemplification. Moreover, finite element analysis of this motor is carried out to investigate the magnetic field distribution at different rotor positions and load currents, in which the leakage flux outside the stator circumference of the DSPM motor is firstly taken into account. Hence, the characteristics of the proposed motor are deduced. Experimental results of the prototype are given to verify the theoretical analysis and to confirm its high efficiency.**

***Index Terms*—Doubly salient motor, finite element analysis, leakage flux, permanent magnet (PM) motor, sizing equation.**

I. INTRODUCTION

AT PRESENT, there is an increasing tendency to consider brushless motors, namely, the permanent magnet (PM) brushless motor and the switched reluctance (SR) motor, for industrial and electric vehicle applications [1], [2]. The PM brushless motor offers the advantages of high power density and high efficiency. However, since its PMs are located in the rotor, this motor suffers from the possibility of irreversible demagnetization by high temperature operation or armature reaction flux. Also, the mechanical integrity of PMs in the rotor inhibits its application at high speeds. On the other hand, the SR motor takes the advantages of simple configuration and mechanical robustness. However, because of the absence of PMs, it generally offers lower efficiency and lower power density than the PM brushless motor. Recently, a new class of brushless motors, termed the doubly salient permanent magnet (DSPM) motor, has been introduced [3], [4]. This DSPM motor incorporates the merits of both the PM brushless motor and the SR motor. First, the corresponding PMs are located in the stator, eliminating the problems of irreversible demagnetization and mechanical instability, while retaining the merits of high efficiency and high power density. Second, the corresponding rotor is the same as that of the SR motor, hence, adopting the advantages of simple configuration and mechanical robustness.

In the development of the DSPM motor, there were a number of publications [3]–[10]. However, most of them were biased on the analysis, rather than the design, of the DSPM motor. Such analyses cannot help the engineers to kick off the design process. In fact, the initial calculation of motor dimensions and parameters, such as the core diameter, stack length, PM size, and winding turns, is crucial. To the best of authors' knowledge, these kinds of calculations are surprisingly rare. Even so, only the outside diameter and the stack length of the DSPM motor were ever discussed [3].

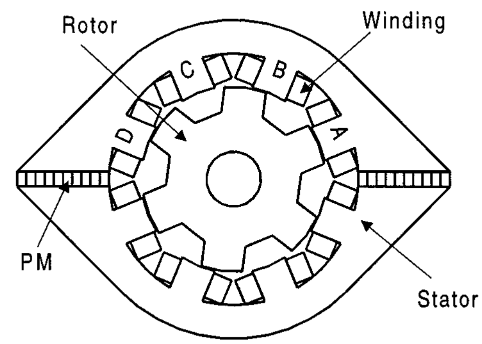

Fig. 1. Proposed four-phase 8/6-pole DSPM motor.

Very recently, a new 8/6-pole DSPM motor has been proposed [8]. It has definite advantages over the 6/4-pole one, namely, higher power density, wider speed range, less torque ripple, and lower current magnitude. Although this DSPM motor possesses simple configuration, it does not imply any simplicity in design and analysis because of the heavy magnetic saturation in pole tips, the fringe effect of poles and slots, as well as the cross coupling between PM flux and armature current flux. The main objective of this paper is to firstly present the design details of the DSPM motor, thus providing the designer a practical way to make initial calculation of motor dimensions and parameters. An 8/6-pole DSPM motor will be used for exemplification. Then, finite element analysis of this motor will be carried out, in which the magnetic saturation and the coupling between PM flux and armature current flux are taken into account. In addition, the leakage flux outside the stator circumference will firstly be considered. Finally, experimental results on the back EMF, inductance, and efficiency will be given to verify the theoretical prediction.

II. THEORY

Fig. 1 shows the cross section of the proposed four-phase 8/6-pole DSPM motor. Under the assumptions that the fringing effect is negligible and the permeability of the core is infinite, a linear variation of PM flux linkage and thus a rectangular back EMF are resulted in each of the stator windings at no-load. The

Manuscript received July 31, 2000; revised February 6, 2001. This work was supported in part by a grant from the RGC Project HKU 7128/99E, Hong Kong, and a grant from NSFC Project 59507001, China.

The authors are with the Department of Electrical and Electronic Engineering, University of Hong Kong, Pokfulam, Hong Kong, China.

Publisher Item Identifier S 0018-9464(01)05164-0.

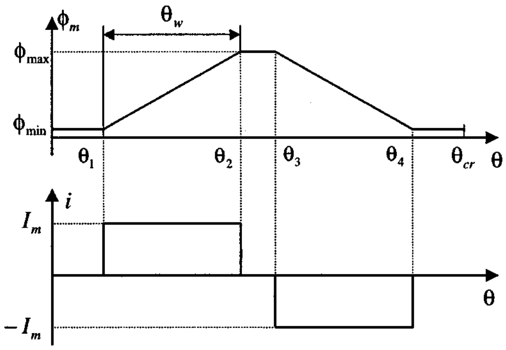

Fig. 2. Theoretical flux and current waveforms.

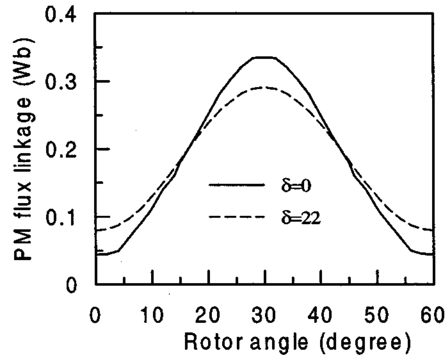

Fig. 3. PM flux linkage versus rotor angle with and without skewing.

corresponding theoretical waveforms of PM flux ϕ_m and phase current i are shown in Fig. 2. Notice that the zero-current interval between the positive and negative currents is purposely provided to ensure successful current reversal. Since the applied voltage U is the phase voltage u of each phase winding, the per-phase input power P can be expressed as

$$\begin{aligned} P &= \frac{1}{T}\int_0^T ui\,dt \\ &= \frac{1}{T}\left[\int_{t_1}^{t_2} UI_m\,dt + \int_{t_3}^{t_4}(-U)(-I_m)\,dt\right] \\ &= \frac{1}{T}\,2UI_m\Delta T \end{aligned} \tag{1}$$

where

T	$= \theta_{cr}/\omega_r$;
ΔT	$= \theta_w/\omega_r$;
$\theta_{cr} = 2\pi/p_r$	rotor pole pitch;
$\theta_w = \theta_2 - \theta_1 = \theta_4 - \theta_3$	angular displacement of a stroke;
p_r	rotor pole number;
ω_r	rotor angular speed;
$t_1 \sim t_4$	time instants corresponding to the rotor positions $\theta_1 \sim \theta_4$.

Thus, (1) can also be expressed as

$$P = 2UI_m\frac{\theta_w}{\theta_{cr}}. \tag{2}$$

When there are m phases, the total input power P_1 becomes

$$P_1 = mP = 2mUI_m\frac{\theta_w}{\theta_{cr}}. \tag{3}$$

Denoting the efficiency as η, the total output power P_2 is written as

$$P_2 = \eta P_1 = 2mUI_m\frac{\theta_w}{\theta_{cr}}\,\eta. \tag{4}$$

Substituting $\theta_{cr} = 2\pi/p_r$ into (4), it yields

$$P_2 = \frac{p_r}{\pi}\,mk_eEI_m\theta_w\eta \tag{5}$$

where $k_e = U/E$, and E is the phase back EMF due to the variation of PM flux linkage. This back EMF can be expressed as

$$E = w\frac{d\phi_m}{d\theta}\,\omega_r \approx w\frac{\phi_{\max}-\phi_{\min}}{\theta_w}\,\omega_r = w\frac{\Delta\phi_m}{\theta_w}\,\omega_r \tag{6}$$

where w is the number of winding turns in series per phase, $\phi_{\max}$ and $\phi_{\min}$ are the PM flux linked by one coil when the stator pole aligns and nonaligns with the rotor pole, respectively. In general, $\Delta\phi_m$ can further be expressed as

$$\begin{aligned} \Delta\phi_m &= \phi_{\max} - \phi_{\min} \approx 0.87\phi_{\max} = 0.87k_d\alpha_s\tau_s l_e B_\delta \\ &= 0.87k_d\alpha_s\frac{\pi D_{si}}{p_s}\,l_e B_\delta \end{aligned} \tag{7}$$

where

k_d	flux leakage factor;
l_e	stack length;
B_δ	airgap flux density;
$\tau_s = \pi D_{si}/p_s$	stator pole pitch;
α_s	stator pole arc factor;
p_s	stator pole number;
D_{si}	stator inner diameter.

Substituting (7) into (6), the back EMF can be written as

$$E = \frac{0.87\pi k_d w\alpha_s D_{si} l_e B_\delta}{p_s\theta_w}\,\omega_r. \tag{8}$$

When the rotor is purposely skewed to minimize the cogging torque, the characteristic of PM flux linkage and hence the back EMF are altered. Fig. 3 shows these characteristics with no skewing ($\delta = 0°$) and with a skewing angle of about one half the stator pole pitch ($\delta = 22°$). In order to take into account the effect of rotor skewing, a skewing factor is defined as

$$k_s = \cos\left(\frac{\pi}{2\theta_{cs}}\,\delta\right) \tag{9}$$

where $\theta_{cs} = 2\pi/p_s$ is the stator pole pitch. Thus, (8) can be modified as

$$E = \frac{0.87\pi k_s k_d\alpha_s D_{si} l_e B_\delta}{p_s\theta_w}\,\omega_r. \tag{10}$$

Notice that $\delta = 0°$ implies no reduction in the back EMF, whereas $\delta = \theta_{cs}$ results in no back EMF.

On the other hand, the magnitude of the rectangular current waveform can be expressed as

$$I_m = k_i I_{\rm rms} = k_i \frac{\pi D_{si} A_s}{2mw} \tag{11}$$

where

A_s electric loading of the stator;
$I_{\rm rms}$ root mean square (RMS) phase current;
k_i $= I_m/I_{\rm rms}$.

Substituting (10), (11), and $\omega_r = 2\pi n_s/60$ into (5) while adopting the general case that $\alpha_s \approx 0.5$, the output power of this DSPM motor can be derived as

$$P_2 = \frac{0.87\pi^2}{120} \frac{p_r}{p_s} k_s k_d k_e k_i A_s B_\delta D_{si}^2 l_e n_s \eta \tag{12}$$

where n_s is the rated speed of the motor.

The output power equation given by (12) reveals the relationships between the output power and various design parameters. Therefore, it is the basis for design and steady-state analysis of the DSPM motor. For instance, it can be found from (12) that the output power is directly proportional to the ratio of rotor to stator poles p_r/p_s. Given A_s and B_δ, the larger the value of p_r/p_s can certainly possess the higher the power density. Hence, the 8/6-pole motor can offer higher power density than the 6/4-pole one by 12.5%.

III. Design

A. Initial Sizing of Core Diameter and Stack Length

By rearranging (12), the sizing equation can be deduced as

$$D_{si}^2 l_e = \frac{P_2}{\frac{0.87\pi^2}{120} \frac{p_r}{p_s} k_s k_d k_e k_i A_s B_\delta n_s \eta}. \tag{13}$$

In accordance with the basic operation of the DSPM motor, the general relationship between p_s, p_r, and m are given by

$$\begin{cases} p_s = 2mk \\ p_r = p_s \pm 2k \end{cases} \tag{14}$$

where k is a positive integer. Thus, $p_s/p_r =$ 6/4, 8/6, and 12/8 are typical configurations of the DSPM motor.

As shown in Fig. 2, it is generally valid that $\theta_w \approx \theta_{cr}/3$ for the DSPM motor. Hence, k_i can be calculated as follows

$$\begin{aligned} I_{\rm rms} &= \sqrt{\frac{1}{T}\int_0^T i^2\,dt} = \sqrt{\frac{1}{\theta_{cr}} 2 I_m^2 \theta_w} \\ &= \sqrt{\frac{2}{\theta_{cr}} \frac{1}{3} \theta_{cr}} I_m = \sqrt{\frac{2}{3}} I_m \end{aligned} \tag{15}$$

$$k_i = \frac{I_m}{I_{\rm rms}} = \sqrt{\frac{3}{2}}. \tag{16}$$

Generally, the ranges of k_d and k_e are given by

$$k_d = 0.90 \sim 0.93 \tag{17}$$

$$k_e = 1.5 \sim 2.0. \tag{18}$$

Since the DSPM motor is a new class of motors, there is a shortage of statistical data on the selection of A_s. Based on our experience, the range of A_s is selected to be $10\,000 \sim 30\,000$ A/m. On the other hand, since the airgap flux density of the DSPM motor is usually the same as the tooth flux density B_δ is generally equal to 1.5 T. Therefore, by substituting $A_s = 15\,000$ A/m, $B_\delta = 1.5$ T, $k_d = 0.9$, $k_e = 1.5$, $k_i = \sqrt{3/2}$, $n_s =$ 1500 rpm, and $\eta = 0.82$ into (13), the main dimensions of the proposed 750-W 8/6-pole DSPM motor with rotor skewing of 20° can be calculated by

$$D_{si}^2 l_e = 4.2717 \times 10^{-4}\ \text{m}^3. \tag{19}$$

Hence, once D_{si} is selected l_e can be deduced from (19). For instance, the main dimensions of the proposed motor are given by

$$\begin{cases} D_{si} = 0.075\ \text{m} \\ l_e = 0.076\ \text{m}. \end{cases} \tag{20}$$

Once the main dimensions are determined, the other structural dimensions, namely the stator outer diameter, pole heights and pole arcs can be specified in a similar way of the SR motor [2], [11].

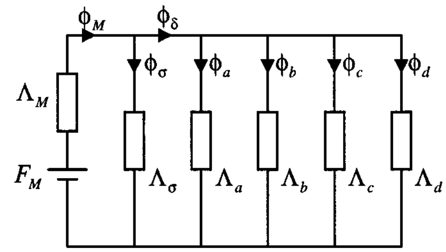

Fig. 4. Simplified equivalent magnetic circuit.

B. Initial Sizing of Permanent Magnets

Fig. 4 shows a simplified equivalent magnetic circuit of the proposed 8/6-pole DSPM motor, in which the iron core is assumed to be of infinite permeability. From the circuit, it yields

$$\phi_a = \phi_\delta \frac{\Lambda_a}{\Lambda_a + \Lambda_b + \Lambda_c + \Lambda_d} = \phi_\delta \frac{\Lambda_a}{\Lambda_\delta} \tag{21}$$

$$\phi_\delta = \phi_M \frac{\Lambda_\delta}{\Lambda_\delta + \Lambda_\sigma} \tag{22}$$

where

$\Lambda_a \sim \Lambda_d$ permeances of phases A D, respectively;
Λ_δ sum of the permeances of four phases;
Λ_σ leakage permeance of PMs;
ϕ_a flux of phase A;
ϕ_δ airgap flux equal to the sum of four phase fluxes;
ϕ_M magnet flux.

Making use of (21) and (22), it deduces

$$\phi_M = \frac{\Lambda_\delta + \Lambda_\sigma}{\Lambda_\delta} \frac{\Lambda_\delta}{\Lambda_a} \phi_a = \sigma \frac{\Lambda_\delta}{\Lambda_a} \phi_a \tag{23}$$

where σ is the magnet leakage factor which is defined as the ratio of magnet flux to airgap flux

$$\sigma = \frac{\phi_M}{\phi_\delta} = \frac{\Lambda_\delta + \Lambda_\sigma}{\Lambda_\delta}. \tag{24}$$

The value of σ depends on the motor configuration. According to finite element analysis, which will be discussed in Section IV, the corresponding value is generally of $1.4 \sim 1.5$.

In (23), the permeances Λ_a and Λ_δ can be expressed as

$$\Lambda_a = \mu_0 \frac{D_{si}\alpha_a l_e}{4g_0} \tag{25}$$

$$\Lambda_\delta = \mu_0 \frac{D_{si}\alpha_\delta l_e}{4g_0} \tag{26}$$

where

- α_a overlapping angle between the stator pole of phase A and a rotor pole;
- α_δ sum of overlapping angles between four phase stator poles and rotor poles;
- g_0 airgap length;
- μ_0 permeability of free space.

When the rotor pole arc β_r is given by

$$\beta_r = 2\theta_{cs} - \theta_{cr} \tag{27}$$

α_δ becomes constant, hence, the operating point of PMs does not change with the rotor position. Even when (27) is not satisfied, the variation of this operating point does not introduce a significant error. So the magnet flux in (23) can be calculated at a particular rotor position that the stator pole of phase A fully aligns with a rotor pole. Namely, as shown in Fig. 1, the flux of phase A has its maximum value $\phi_{a\,\max}$. Then, α_δ and α_a can be expressed as

$$\alpha_\delta = 2\beta_s + \beta_r + \theta_{cr} - 2\theta_{cs} \tag{28}$$

$$\alpha_a = \max(\beta_s, \beta_r) = \beta_s. \tag{29}$$

Substituting (25) and (26) into (23) and making use of (28) and (29), it deduces

$$\phi_M = \frac{\sigma B_\delta D_{si} l_e}{2}(2\beta_s + \beta_r + \theta_{cr} - 2\theta_{cs}). \tag{30}$$

When adopting neodymium–iron–boron (Nd–Fe–B) as the PM material for the proposed DSPM motor, the demagnetizing characteristic of PMs is almost linear. As shown in Fig. 5, it yields

$$B_M = B_r\left(1 - \frac{H_M}{H_c}\right) \tag{31}$$

$$H_M = H_c\left(1 - \frac{B_M}{B_r}\right) \tag{32}$$

where B_M and H_M are, respectively, the flux density and field strength of PMs at the operating point, while B_r and H_c are, respectively, the remnant flux density and coercive force of PMs. Also, by using Ampere's Law, it yields

$$H_M h_{pm} = 2H_\delta g_0 \tag{33}$$

where H_δ is the field strength in airgap, and h_{pm} is the magnet thickness in the direction of magnetization. From (32) and (33), it deduces

$$h_{pm} = \frac{2B_\delta g_0}{\mu_0 H_c\left(1 - \dfrac{B_M}{B_r}\right)}. \tag{34}$$

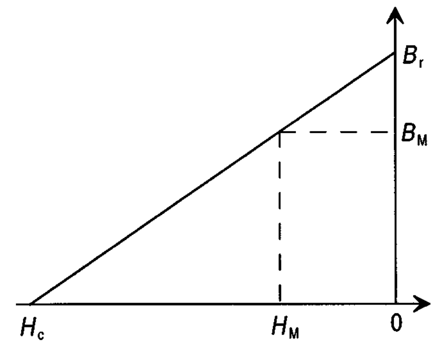

Fig. 5. Demagnetizing characteristics of PMs.

Typically, the value of B_M/B_r is 0.7∼0.95 [12]. By using (30), the surface area S_{pm} of each piece of PMs can be expressed as

$$S_{pm} = \frac{\phi_M}{2B_M} = \frac{\sigma B_\delta D_{si} l_e}{4B_M}(2\beta_s + \beta_r + \theta_{cr} - 2\theta_{cs}). \tag{35}$$

As the magnet length l_{pm} in the axial direction is usually the same as the stack length, the magnet width w_{pm} can be expressed as

$$w_{pm} = \frac{S_{pm}}{l_{pm}} = \sigma\frac{B_\delta D_{si}}{4B_M}(2\beta_s + \beta_r + \theta_{cr} - 2\theta_{cs}). \tag{36}$$

In the proposed motor, PMs with $B_r = 1.08$ T and $H_c = 843521$ A/m (10600 Oe) are used. By substituting $B_\delta = 1.5$ T, $g_0 = 0.00045$ m, $H_c = 843521$ A/m, and $B_M/B_r = 0.8$ into (34), h_{pm} can be obtained as

$$h_{pm} = 6.37 \times 10^{-3}\ \text{m}. \tag{37}$$

Also, by substituting $\sigma = 1.5$, $B_\delta = 1.5$ T, $D_{si} = 0.075$ m, $B_M = 0.8B_r = 0.864$ T, $\beta_s = 0.384$, $\beta_r = 0.454$, $\theta_{cr} = \pi/3$, and $\theta_{cs} = \pi/4$ into (36), w_{pm} can be obtained as

$$w_{pm} = 0.034\ \text{m}. \tag{38}$$

C. Initial Calculation of Winding Turns

The electromagnetic torque for one-phase-on operation of the proposed DSPM motor can be written as

$$T_{ph} = i\frac{d\psi_{pm}}{d\theta} + \frac{1}{2}i^2\frac{dL}{d\theta} = T_{pm} + T_r \tag{39}$$

where

- T_{ph} instantaneous electromagnetic torque per phase;
- T_{pm} PM torque component due to the interaction between PM flux linkage and armature current;
- T_r reluctance torque component due to the variation of reluctance;
- ψ_{pm} PM flux linkage;
- L phase inductance.

When the rectangular current waveform, as shown in Fig. 2, is applied to the phase winding, the average value of the reluctance torque component is equal to zero because of the symmetric inductance characteristic with respect to the rotor position angle.

Thus, the average torque per phase is governed by the average value of the PM torque component only, which is given by

$$T_{avph} = \frac{1}{\theta_{cr}} \int_0^{\theta_{cr}} \left(i \frac{d\psi_{pm}}{d\theta} \right) d\theta = \frac{2}{\theta_{cr}} I_m \Delta\phi_m w \tag{40}$$

where I_m is the magnitude of the rectangular current waveform. Hence, the total average torque T_{av} of m phases is given by

$$T_{av} = \frac{2m}{\theta_{cr}} I_m \Delta\phi_m w. \tag{41}$$

When neglecting the friction and windage losses, it yields

$$T_{av} \frac{2\pi n_s}{60} = P_2. \tag{42}$$

Substituting (4) and (41) into (42), it deduces

$$w = \frac{U\theta_w \eta}{\Delta\phi_m \frac{2\pi n_s}{60}}. \tag{43}$$

By substituting (7) into (43), the number of winding turns per phase can be obtained as

$$w = \frac{U\theta_w \eta}{0.87 k_d \frac{\alpha_s \pi D_{si}}{p_s} l_e B_\delta \frac{2\pi n_s}{60}}. \tag{44}$$

It should be noted that (44) is obtained based on the ideal rectangular current waveform. Since the realistic current waveform is trapezoidal rather than rectangular, the corresponding θ_w is usually smaller than the ideal θ_w. Hence, the number of winding turns calculated by (44) is usually larger than the actual one. Our experiences in the design of 6/4-, 8/6-, and 12/8-pole DSPM motors indicate that 80% of the value given by (44) is close to the actual value. Therefore, taking into account the correction factor of 0.8, the modified number of winding turns is expressed as

$$w' = \frac{0.8 U\theta_w \eta}{0.87 k_d \frac{\alpha_s \pi D_{si}}{p_s} l_e \frac{2\pi n_s}{60}}. \tag{45}$$

Based on the above design procedure, the dimensions and parameters of the proposed 8/6-pole DSPM motor are obtained. The major design data are listed in Table I. The corresponding prototype is shown in Fig. 6.

IV. Finite Element Analysis

Having completed the design process, the finite element method is employed to analyze the magnetic field distribution of the proposed DSPM motor. Due to the semiperiodic motor configuration, the region of interests for finite element analysis (FEA) is one half of the whole motor cross-section. Since the PMs are located in the stator, the leakage flux outside the stator circumference (which is generally neglected in the conventional PM brushless motor) becomes significant. In order to take this leakage flux into account, the domain of the region under consideration is extended from the stator circumference to the surrounding space with a radius R_o as shown in Fig. 7.

TABLE I
Design Data of 8/6-Pole DSPM Motor

Stator outer diameter (mm)	128
Stator inner diameter (mm)	75
Stack length (mm)	75
Airgap length (mm)	0.45
Rotor inner diameter (mm)	22
Number of phases	4
Stator pole number	8
Rotor pole number	6
Stator pole arc (degree)	22
Rotor pole arc (degree)	26
Stator pole depth (mm)	13
Rotor pole depth (mm)	10
Number of turns/phase	220
Rated speed (rpm)	1500
Magnet volume (mm^3)	$2\times(6\times37\times75)$

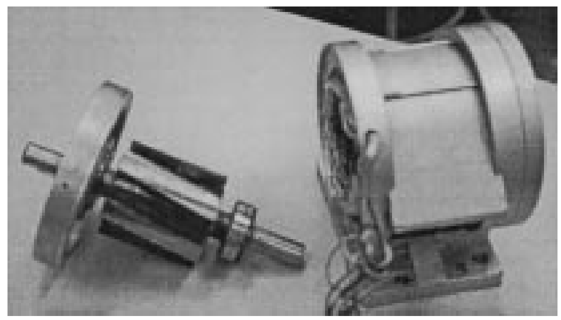

Fig. 6. Experimental DSPM motor.

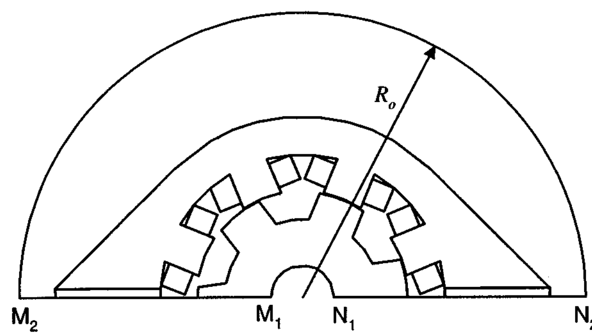

Fig. 7. Domain of the region.

Fig. 8 shows the generated mesh for FEA. The corresponding Maxwell's equation is expressed as [13], [14]

$$\frac{\partial}{\partial x}\left(\nu \frac{\partial A_z}{\partial x}\right) + \frac{\partial}{\partial y}\left(\nu \frac{\partial A_z}{\partial y}\right) = -(J_z + J_{pm}) \tag{46}$$

where

A_z and J_z	z components of magnetic vector potential $\mathbf{A}$ and current density $\mathbf{J}$, respectively;
J_{pm}	equivalent surface current density of PMs;
ν	reluctivity.

The corresponding boundary conditions are given by

$$\mathbf{A}|_{M_1N_1} = \mathbf{A}|_{M_2N_2} = 0 \tag{47}$$

$$\mathbf{A}|_{M_1M_2} = -\mathbf{A}|_{N_1N_2}. \tag{48}$$

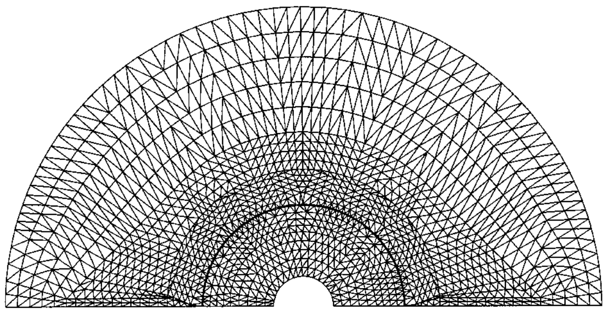

Fig. 8. Generated mesh.

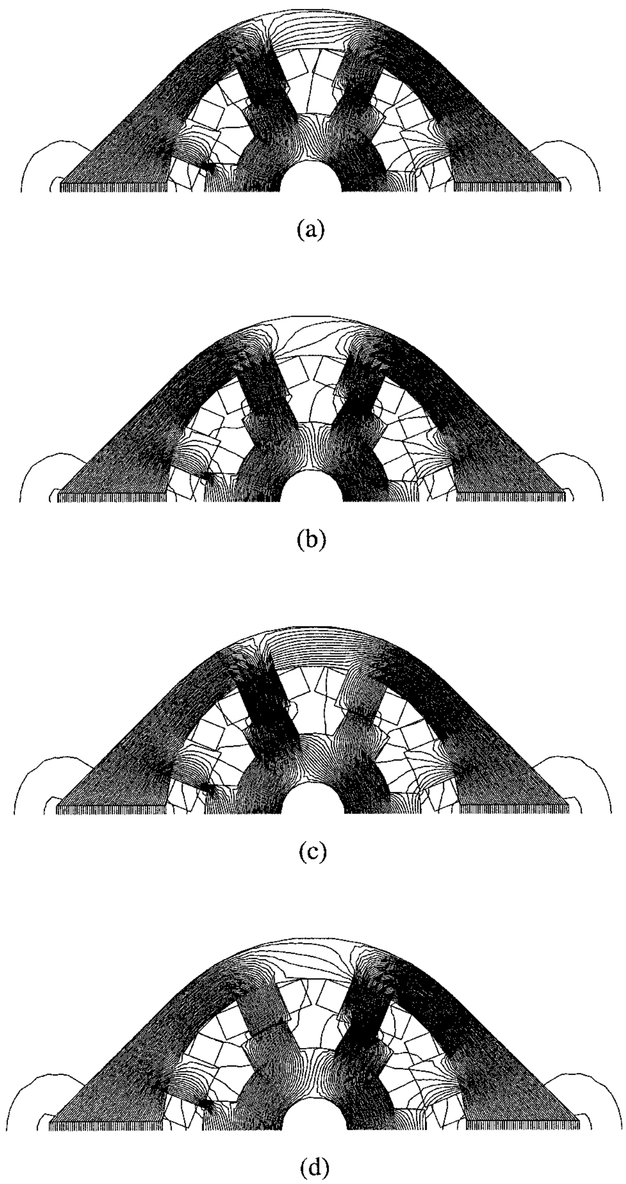

Fig. 9. Magnetic field distributions at $\theta_b = 20^\circ$. (a) PMs only, (b) PMs and i_b=2A, (c) PMs and $i_b = -2$ A, and (d) PMs, $i_b = 2$ A and $i_c = -2$A.

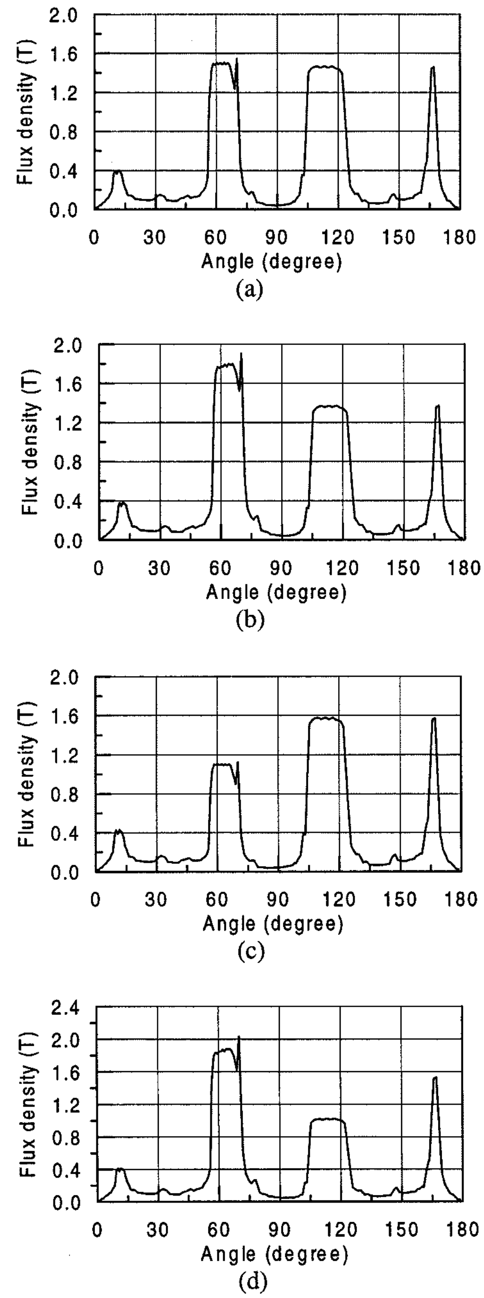

Fig. 10. Airgap flux density distributions at $\theta_b = 20^\circ$. (a) PMs only, (b) PMs and $i_b = 2$ A, (c) PMs and $i_b = -2$ A, and (d) PMs, $i_b = 2$ A and $i_c = -2$ A.

The magnetic field distributions of the DSPM motor at different load conditions and rotor position angles are analyzed. Fig. 9 shows the distributions at the instant that the rotor position angle with respect to the phase B is 20°, in which Fig. 9(a) is the field produced by the PMs only, Fig. 9(b) the field by the PMs and positive armature current i_b (strengthening effect), Fig. 9(c) is the field by the PMs and negative armature current i_b (weakening effect), and Fig. 9(d) the field by the PMs, positive armature current i_b and negative armature current i_c. The corresponding magnetic flux density distributions in the airgap are shown in Fig. 10.

As shown in Fig. 10, it can be found that the airgap flux density under the stator pole is about 1.5 T at no-load. In case the phase B conducts a current of 2 A, which strengthens the field of PMs, the airgap flux density under the conducting pole is increased whereas that under the nonconducting pole is decreased and vice versa. A similar phenomenon occurs in the case of two-phase conduction. Nevertheless, the sum of the effective

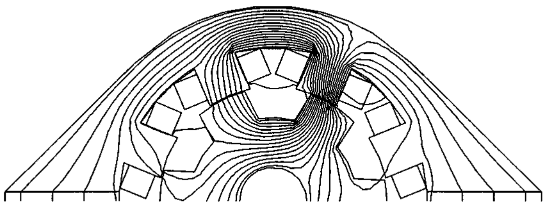

Fig. 11. Armature field distribution at $\theta_b = 20°$ and $i_b = 2$ A.

TABLE II
EFFECT OF R_o ON AIRGAP FLUX

	$R_0 = R_{so} = 64$ mm	$R_o = 95$ mm	$R_o = 110$ mm	$R_o = 120$ mm
ϕ_a (mWb)	0.84294	0.82856	0.82219	0.82041
ϕ_b (mWb)	1.52116	1.50120	1.49168	1.48948
ϕ_c (mWb)	0.81858	0.80493	0.79845	0.79696
ϕ_d (mWb)	0.24180	0.23456	0.23164	0.23112
$\phi_\delta = \sum_{i=a}^{d} \phi_i$	3.42448	3.36925	3.34396	3.33797

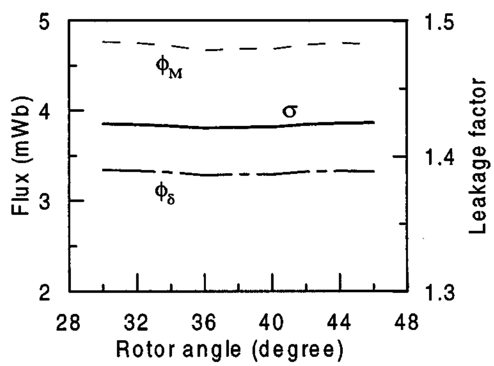

Fig. 12. Fluxes and magnet leakage factor versus rotor angle.

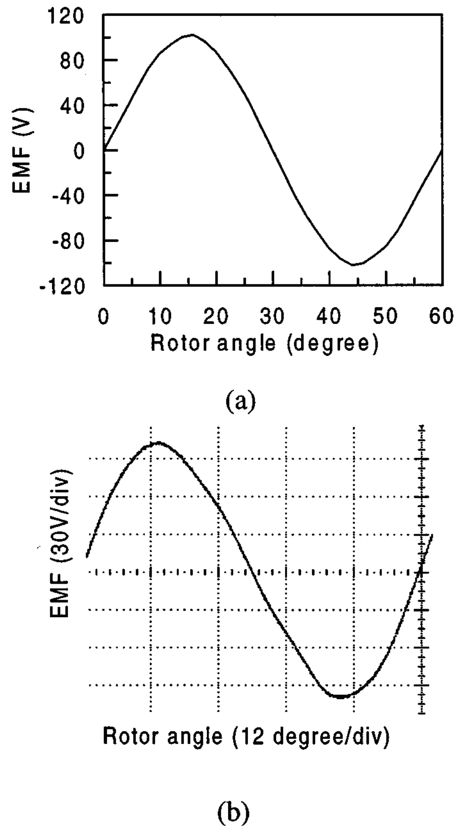

Fig. 13. EMF waveforms at 1500 rpm. (a) Predicted and (b) measured.

flux of the four phases does not significantly change, indicating that the airgap flux in the DSPM motor is mainly contributed by PMs. This illustrates that the strengthening or weakening action of the armature reaction flux to the PM flux is insignificant. The reason can be observed from Fig. 11, in which most of the armature flux loops through adjacent stator poles, and only a little portion passes through the PMs.

To explore the effect of R_o on the field analysis, the magnetic field distributions at different values of R_o are calculated. Table II lists the calculated airgap fluxes ϕ_δ when $R_o = 64$ mm (the conventional boundary that is equal to the stator outer radius R_{so}), $R_o = 95$ mm, $R_o = 110$ mm, and $R_o = 120$ mm. Since the discrepancy of ϕ_δ between $R_o = 95$ mm and $R_o = 110$ mm is 0.76%, while that between $R_o = 110$ mm and $R_o = 120$ mm is only 0.18%, $R_o = 110$ mm is considered to be a reasonable selection for the proposed DSPM motor. Comparing ϕ_δ between $R_o = 110$ mm and $R_o = 64$ mm, it can be found that the effective airgap flux is reduced by 2.6%, which illustrates that the leakage flux outside the stator circumference should be taken into account.

Moreover, Fig. 12 shows the magnet flux ϕ_M, the airgap flux ϕ_δ, and hence, the magnet leakage factor σ when the rotor rotates from the position that the pole of phase B aligns with a rotor pole to the position that the pole of phase C aligns with a rotor pole. It can be seen that the magnet leakage factor of this 8/6-pole DSPM motor almost keeps constant at 1.42. Additionally, both the magnet and airgap fluxes do not exhibit significant variations with the rotor position even though the rotor pole arc of the 8/6-pole motor can not satisfy (27). Hence, the assumption of neglecting the variation of the PM operating point with respect to the rotor position made in Section III-B is reasonable.

V. CHARACTERISTICS

A. PM Flux Linkage and EMF

The PM flux linkage versus rotor angle can be obtained from the finite element analysis as shown in Fig. 3. Then, the back EMF can readily be deduced by

$$e = \frac{d\psi_{pm}}{dt} = \frac{d\psi_{pm}}{d\theta}\,\omega_r. \tag{49}$$

Fig. 13 shows the predicted and measured back EMF waveforms of the 8/6-pole prototype, respectively. It illustrates that the experimental result closely agrees with the theoretical one.

B. Inductance

In the calculation of inductance, the cross coupling between PM flux and armature flux is taken into account. Both the PM flux and armature flux contribute the total flux linkage ι as given by

$$\psi = \psi_{pm} + Li. \tag{50}$$

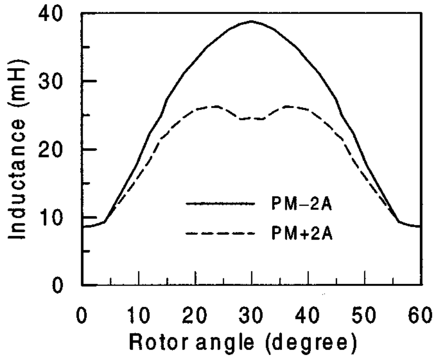

Fig. 14. Inductance versus rotor angle.

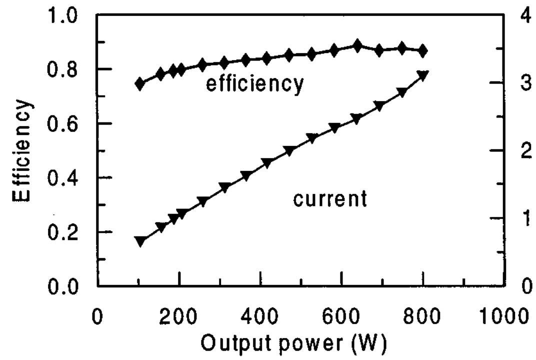

Fig. 15. Measured efficiency and RMS current at rated speed.

TABLE III
COMPARISON OF INDUCTANCE

θ	Calculated (mH)			Measured (mH)		
	L^+	L^-	L	L^+	L^-	L
0°	8.63	8.62	8.63	8.77	9.08	8.93
15°	24.03	26.93	25.48	21.7	26.81	24.26
30°	28.15	36.67	32.41	29.05	36.88	32.97

Due to magnetic saturation, the inductance L is both position-dependent and current-dependent. Thus, in order to determine the inductance, the finite-element analysis is carried out in two steps. First, no current is applied to the phase winding, so that the flux linkage is solely due to PMs $\psi = \psi_{pm}$. Second, the current i is applied to the phase winding, thus the inductance is given by

$$L = \frac{\psi - \psi_{pm}}{i}. \tag{51}$$

Hence, Fig. 14 shows the inductance characteristics of the proposed DSPM motor, where "PM + 2 A" and "PM − 2 A" denote the strengthening and weakening actions of the armature flux (with the phase current of 2 A) to the PM flux, respectively. It is noted that the inductance under "PM + 2 A" is lower than that under "PM − 2 A" because of higher saturation under "PM + 2 A." Moreover, Table III gives a comparison of the predicted and measured inductances with the phase current of 1 A, in which L^+, L^-, and $L = (L^+ + L^-)/2$ denote the corresponding maximum, minimum, and average values, respectively. As expected, the agreement is good.

It will be noted that the inductance of the DSPM motor is generally much lower than that of the SR motor due to the fact that the permeability of PMs is similar to that of air. Actually, a lower inductance is preferred because it reduces not only the electrical time constant, but also the torque ripple generated by the reluctance torque component as given in (39).

C. Efficiency

A microcomputer-based controller and a power converter are designed and built to drive the proposed DSPM motor. A DC dynamometer is mechanically coupled to the motor as an adjustable load. Both the input power and RMS current of the motor are measured by a digital power analyzer. Hence, the measured efficiency and current of the proposed motor operating at the rated speed of 1500 rpm are shown in Fig. 15. It can be found that the motor offers high efficiencies over a wide range of output power, which is highly desirable for application to electric vehicles. The efficiency at the rated operating point is 87.7%, which is much higher than that of an induction motor (typically 75%) with the same capacity and speed range.

VI. CONCLUSION

In this paper, the design and analysis of a new DSPM motor has been presented. Based on the derived output power equation, the sizing equation and the relationships between the main design parameters and performance requirements are established, providing a practical way for the designer to make initial calculations of the motor frame, PM size, and winding turns. An 8/6-pole DSPM motor has been designed and built for evaluation. Moreover, the finite element analysis of the proposed DSPM motor has been carried out, in which the leakage flux outside the stator circumference is firstly taken into account. Hence, the characteristics of the motor have been deduced. The experimental results have verified the theoretical analysis and confirmed the high efficiency nature (rated at 87.7%) of the proposed motor. Finally, its key features are summarized as follows.

- The airgap flux of the DSPM motor is mainly contributed by PMs, whereas the armature current contributes to change the flux distribution.
- Because most of the armature flux loops through the adjacent stator poles, not through PMs, the DSPM motor is less sensitive to demagnetization than other PM brushless motors.
- The inductance of the DSPM motor depends not only on the rotor position, but also on the strengthening/weakening action of the armature field to the PM field.
- The leakage flux outside the stator circumference of the DSPM motor should be taken into account, which may lead to a reduction in the effective flux of about 3%.

REFERENCES

[1] C. C. Chan, K. T. Chau, J. Z. Jiang, W. Xia, M. Zhu, and R. Zhang, "Novel permanent magnet motor drives for electric vehicles," *IEEE Trans. Ind. Electron.*, vol. 43, pp. 331–339, Apr. 1996.
[2] C. C. Chan, Q. Jiang, Y. J. Zhan, and K. T. Chau, "A high-performance switched reluctance drive for P-star EV project," in *Proc. Int. Elect. Vehicle Symp.*, Osaka, Japan, 1996, pp. 78–83.

[3] Y. Liao and T. A. Lipo, "Sizing and optimal design of doubly salient permanent magnet motors," in *Proc. Int. Conf. Electronic Machines and Drives*, London, U.K., 1993, pp. 452–456.
[4] Y. Liao, F. Liang, and T. A. Lipo, "A novel permanent magnet motor with doubly salient structure," *IEEE Trans. Ind. Applicat.*, vol. 31, pp. 1069–1078, Sept./Oct. 1995.
[5] F. Blaabjerg, L. Christensen, P. O. Rasmussen, L. Oestergaard, and P. Pedersen, "New advanced control methods for doubly salient permanent magnet motor," in *Conf. Record 30th IEEE IAS Annual Meeting*, Orlando, FL, 1995, pp. 272–230.
[6] M. M. Radulescu, C. Martis, and K. Biro, "A new electrically-commutated doubly-salient permanent-magnet small motor," in *Proc. 7th Int. Conf. Electrical Machines and Drives*, Durham, U.K., 1995, pp. 213–216.
[7] C. Martis, M. M. Radulescu, and K. Biro, "On the dynamic model of a doubly-salient permanent magnet motor," in *Proc. Mediterranean Electrotechnical Conf.*, Tel-Aviv, Israel, 1998, pp. 410–414.
[8] K. T. Chau, M. Cheng, and C. C. Chan, "Performance analysis of 8/6-pole doubly salient permanent magnet motor," *Elect. Machines and Power Syst.*, vol. 27, no. 10, pp. 1055–1067, 1999.
[9] M. Cheng, K. T. Chau, C. C. Chan, E. Zhou, and X. Huang, "Nonlinear varying-network magnetic circuit analysis for doubly salient permanent magnet motors," *IEEE Trans. Magn.*, vol. 36, pp. 339–348, Jan. 2000.
[10] M. Cheng, K. T. Chau, C. C. Chan, and E. Zhou, "Performance analysis of split-winding doubly salient permanent magnet motor for wide speed operation," *Elect. Machines and Power Syst.*, vol. 28, no. 3, pp. 277–288, 2000.
[11] C. C. Chan, Q. Jiang, and E. Zhou, "A new method of dimension optimization of switched reluctance motors," in *Proc. Chinese Int. Conf. Electronic Machines*, Hangzhou, China, 1995, pp. 1004–1009.
[12] J. R. Hendershot Jr. and T. J. E. Miller, *Design of Brushless Permanent-Magnet Motors*. Oxford, U.K.: Clarendon, 1994.
[13] M. V. K. Chari, G. Bedrosian, J. D'Angelo, and A. Konrad, "Finite element application in electrical engineering," *IEEE Trans. Magn.*, vol. 29, pp. 1306–1314, Feb. 1993.
[14] M. A. Rahman and P. Zhou, "Determination of saturated parameters of PM motors using loading magnetic fields," *IEEE Trans. Magn.*, vol. 27, pp. 3947–3950, May 1991.

Ming Cheng was born in Jiangsu Province, China. He received the B.Sc. and M.Sc. (Eng.) degrees in electrical engineering from Southeast University, Nanjing, China in 1982 and 1987, respectively. He is currently working toward the Ph.D. (Eng.) degree at the University of Hong Kong, Pokfulam, Hong Kong, China.

He was an Associate Professor with the Department of Electrical Engineering, Southeast University, Nanjing, China. His areas of interests include electrical machine and drive design, modeling, simulation, PM machines, and power electronics. He has published some 30 papers in this area. He is the recipient or co-recipient of several Chinese patents.

K. T. Chau (M'89) received the B.Sc. (Eng.) (first-class hons.), M.Phil., and Ph.D. degrees in electrical and electronic engineering from the University of Hong Kong, Pokfulam, Hong Kong, China.

He is currently an Associate Professor with the University of Hong Kong. His teaching and research interests focus on three main areas: power converters, machines and drives, and electric vehicles. In these areas, he has published over a hundred refereed technical papers and some industrial reports.

Dr. Chau has served as Chair and Organizing Committee Members for many international conferences. His biography is listed in *Who's Who in Science and Engineering 1998–1999*.

C. C. Chan (M'77–SM'77–F'92) received the B.Sc. degree from China University of Mining and Technology, Beijing, China, in 1953, the M.Sc. degree from Tsinghua University, Beijing, China,in 1957, and the Ph.D. degree from the University of Hong Kong, Hong Kong, in 1981. He was awarded the Honorary D.Sc. degree from the University of Odessa, Ukraine, in 1992.

He is currently Chair Professor with the Department of Electrical and Electronic Engineering, University of Hong Kong, Pokfulam, Hong Kong, China. He has authored four books, published over 120 technical papers, and holds seven patents.

Prof. Chan is a Fellow of the Royal Academy of Engineering, U.K., an Academician of the Chinese Academy of Engineering, and a Fellow of the Ukraine Academy of Engineering Science.